CrossMark

Effect of Ag Loading on the Microstructure of TiO_2 Electrospun Nanofibers

Zaira Batool[1] · M. Raffi[2] · M. Zakria[2] ·
Rana I. Shakoor[4] · R. Rashid[2] · Mazhar Mehmood[3] ·
Muhammad Aslam Mirza[1]

Abstract In this research work, crystalline structure, phase transformation, morphology and mean size of titanium dioxide (TiO_2) electrospun nanofibers have been tailored by loading with 2.5, 5.0 and 7.5 wt.% of silver (Ag) which was followed by calcination. The as prepared non woven mats of nanofibers were calcinated at 500 °C to allow the reaction moieties to leave the TiO_2 matrix and subsequently formation of Ag clusters. The effect of Ag loading and calcination on the transformation of microstructure of these electrospun nanofibers have been characterized by XRD, FESEM, FT-IR and Raman spectroscopy (RS). The mean diameter of Ag loaded nanofibers has been found to decrease upon calcination which was estimated to 70 nm whereas length was in the order of mm range. XRD and RS results have strongly supported the transformation of crystalline phase from rutile (A) to anatase (R) above 2.5 wt.% of Ag loading in TiO_2 after calcination. The roughness on the outer surfaces of these nanofibers has been observed to increase with the Ag loading consequent to calcination, which has been attributed to the formation Ag nanoparticles that were found adsorbed at the surfaces. An interesting finding of this study is the existence of 1D nanofibers' structure even at higher (7.5 wt.%) Ag loading, as observed by the SEM micrographs.

✉ M. Raffi
    muhammad_raffi@hotmail.com

[1] Department of Chemistry, Mirpur University of Science and Technology (MUST), Mirpur (AJK) 10250, Pakistan

[2] Department of Materials Engineering, National Institute of Lasers and Optronics (NILOP), Islamabad 45650, Pakistan

[3] Department of Materials and Metallurgy, Pakistan Institute of Engineering and Applied Sciences (PIEAS), Islamabad 45650, Pakistan

[4] Department of Mechatronics Engineering, Air University, Sector E-9, Islamabad, Pakistan

Introduction

Titanium dioxide (TiO_2) exists in three crystalline phases; anatase (A), rutile (R), and brookite (B). A and R have tetragonal while B-phase has orthorhombic crystalline structure [1]. The most commonly used crystalline polymorphs of TiO_2 are metastable A and stable R. These polymorphs exhibit inconsistent properties and consequently different photocatalytic performances. The kinetics of these processes is typically considered in terms of temperature and time. A-phase transforms irreversibly to R at elevated temperatures. In case of the former, pure bulk A starts converting irreversibly to R in the air at 600 °C. A-phase is stable at 500 °C and has larger band gap than the R [2–5]. A longer electron–hole pair life in A than in R-phase would make it more likely for charge carriers to participate in surface reactions. One evidence for longer charge carrier lifetimes in A than in R comes from transient photoconductivity measurements on single crystalline samples. [6]. Control in A and R-phases is significant due to their substantial electrical and optical features. A-phase is generally employed in catalysis and catalytic supports owing to its chemically and optically active characteristics [2]. R-phase in TiO_2 has a high refractive index and ultraviolet (UV) absorption characteristics which makes it a favorable material for use in cosmetics, high quality paints and UV absorbents [7]. As a consequence of distortion in each TiO_2 octahedral as well in the group patterns of the octahedral chains result into emergence of three crystal structures.

There are foremost applications of TiO_2 based materials such as photocatalysis, photovoltaic, sensing and photonic crystals [8]. The high recombination rate of photo-induced electron–hole pairs in the photocatalytic processes and absorption capacity of visible light limited the efficiency of a photocatalytic reaction. Therefore, to induce the bathochromic shift, which causes the transfer of optical response from UV to visible range, various approaches have been adopted like doping of transition/noble metals, composite semiconductors, and photosensitization [9]. The metallic doping in TiO_2 can produce trap states, which capture the photo-induced electrons or holes leading to reduced electron–hole recombination in the photocatalytic process and boost the absorption capability of the visible light spectrum [10]. Some noble metals like Pt, Pd, Rh, and Au are too expensive which limit their large scale use at the commercial level. Contrarily, Ag is a cheap metal that has led to a growing interest in the research on Ag-loaded TiO_2 systems [11]. Furthermore, surface plasmon resonance (SPR) of Ag nanostructures present in the TiO_2 nanofibers is expected to increase linearly. The increased strength of SPR raise the local electric field; facilitating the electron–hole production, which ultimately increase the absorption in the visible spectrum [12].

A number of pathways have been developed to prepare loaded and pristine TiO_2 nanofibers [13]. However, in this work electrospinning technique has been used which is technically sound, environment friendly, cost-effective and viable method for synthesizing TiO_2 nanofibers at room temperature and pressure [14]. Research

groups have already prepared pure inorganic nanofibers comprising of the TiO$_2$ [15]. In our study, pristine and Ag-loaded TiO$_2$ nanofibers have been prepared by electrospinning method to control the recombination and phase transformation in them as a function of Ag loading. Herein, main focus is the structuring of physical properties and stability of 1D nanofibers for higher Ag content. In this way, nanofibers have been synthesized which retained their 1D fibrous feature even at 7.5 wt.% of Ag loading. The as prepared and heat treated samples of pristine and Ag-loaded TiO$_2$ nanofibers have been characterized by FT-IR, XRD, Raman spectroscopy (RS)and FE-SEM to investigate their structural and morphological features. Moreover, the influence of Ag loading on the phase transformation of TiO$_2$ electrospun nanofibers, as well on their optical phonon modes, shape, mean size and crystallite growth have been carried out.

Materials and Methods

The as-purchased precursors poly vinylpyrolidone (PVP; MW = 1,300,000, 98%), Titanium isopropoxide (TiP; MW = 284.26, 98%), ethanol (94–96%) of Aldrich company, silver nitrate (99.9%) by Sigma-Aldrich, and acetic acid (99.7%) by Alfa Aesar have been used in the specific ratios for this research. Solution A was prepared by dissolving 0.6 g of TiP in acetic acid and ethanol of 1.2 mL each, which was followed by magnetic stirring (WiseStir, Germany) at room temperature for 10 min. The solution A was mixed with the solution B which was made up of 0.18 g PVP in 3 mL of ethanol. The resultant solution was magnetically stirred for 1 h. This solution was immediately loaded into a 1 mL plastic syringe equipped with a 23 gauge SS needle for electrospinning. The syringe filled with the solution was fixed on an in house made syringe pump (Parker Position System, USA) in such a way that the effusion rate of the solution through the needle was adjusted to 0.6 mL h^{-1}. A vertically aligned circular shaped copper plate (diameter 20 cm) wrapped with aluminum foil was placed at a distance of 12 cm from the tip of the needle which has been used as a grounded collector for the accumulation of nanofibers. The needle of the syringe was connected to the positive terminal of a 50 kV high-voltage DC power supply (DEL Electronic Corporation, USA). A voltage of 18 kV (dc) was applied between needle and the grounded copper collector plate. The electrospinning process was performed at ambient temperature and pressure to synthesize pristine TiO$_2$ nanofibers. These nanofibers were heat treated in the box furnace (KSL-1200X-J, USA) at 500 °C for 3 h at a heating rate of 5 °C min^{-1} to remove the PVP and other moieties. To load TiO$_2$ nanofibers with Ag, silver nitrate (AgNO$_3$) was added into the solution B in the ratios of 2.5, 5.0 and 7.5 wt.% of TIP respectively and stirred for 30 min. Afterwards, this solution was mixed with solution A and the resultant solution was magnetically stirred for 2 h. The schematics of the experimental procedure are shown in Fig. 1. The similar experimental conditions were maintained for making nanofiber samples loaded with Ag.

The morphology of these electrospun nanofibers was observed by the scanning electron microscope (SEM) (FORMAT JEOL/EO, version 1.1). The crystalline
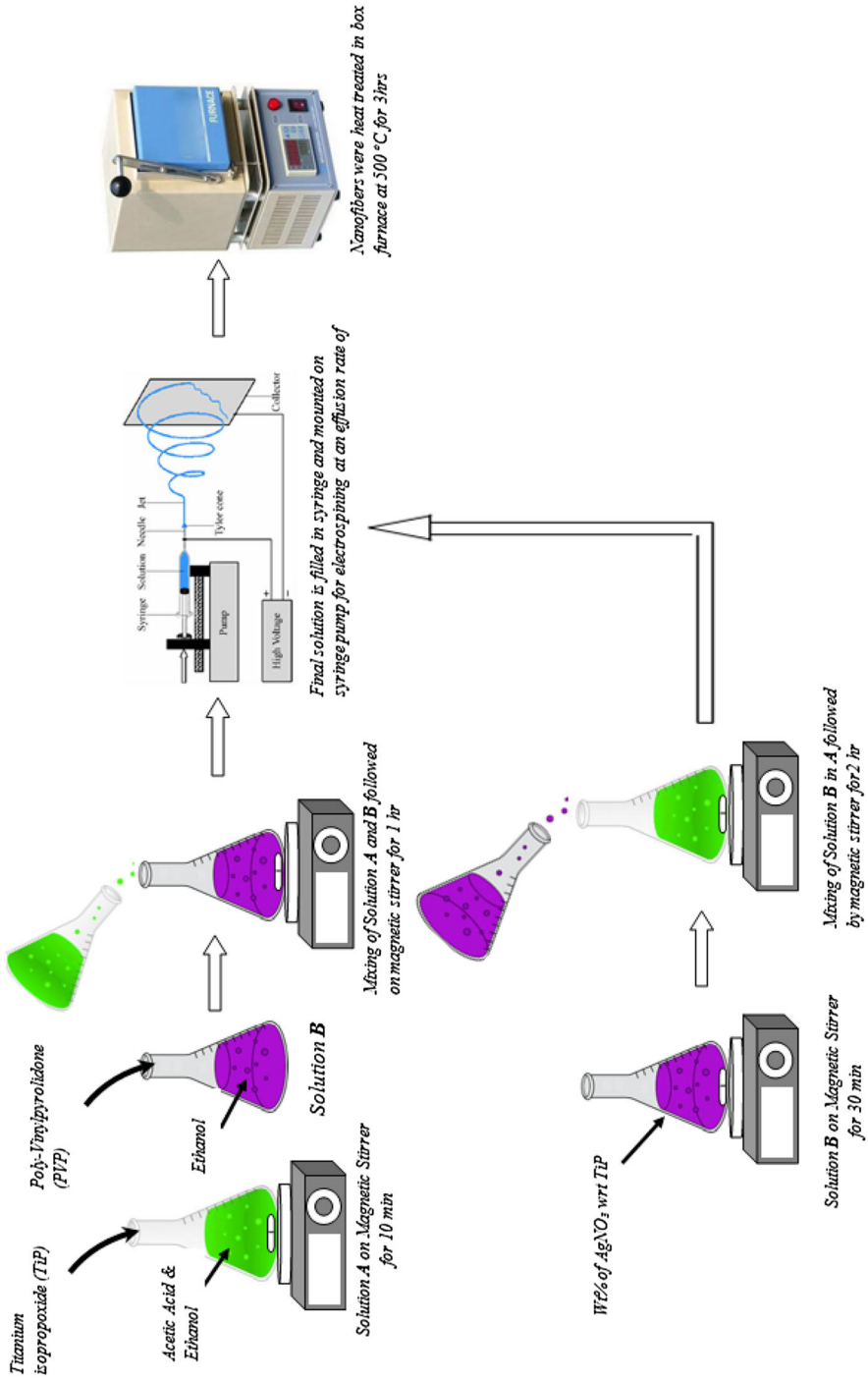
Fig. 1 Schematics of the experimental method

structure and phase transformation in these nanofibers have been evaluated by X-ray diffraction analysis performed in the 2θ range of 20°–90° by using diffractometer (Bruker D-8 Discover HR-XRD) equipped with CuK$_\alpha$ ($\lambda = 1.5418$Å) x-ray radiation source. Fourier transform infrared (FTIR) spectroscopic analysis was carried out on these samples by using FTIR-ATR spectrometer (Thermo Nicolet 6700) in the spectral range 4000–400 cm^{-1} at a resolution of 6 cm^{-1}. Raman spectra were recorded on the spectrometer (DongWoo Optron MST-4000A, S. Korea) equipped with a 532 nm laser excitation source. While performing Raman analysis on these samples, the exposure time was kept 7 s, number of accumulations was 5 whereas laser power was fixed at 20 mW.

## Results and Discussion

Scanning Electron Microscopy (SEM) Analysis

The SEM micrographs of as-spun pristine and Ag-loaded TiO₂ nanofibers and their mean size distribution are shown in Figs. 2 and 3 respectively. Figures 4 and 5 display the micrographs and mean size distribution of pure and Ag-loaded TiO₂ nanofibers calcined at 500 °C. The working distance while performing SEM analysis on these samples varied from 4.1 to 5.3 mm. The micrographs revealed that these nanofibers have maintained smooth and uniform surfaces with non-woven orientations over the collector surface. From these images, it has been observed that
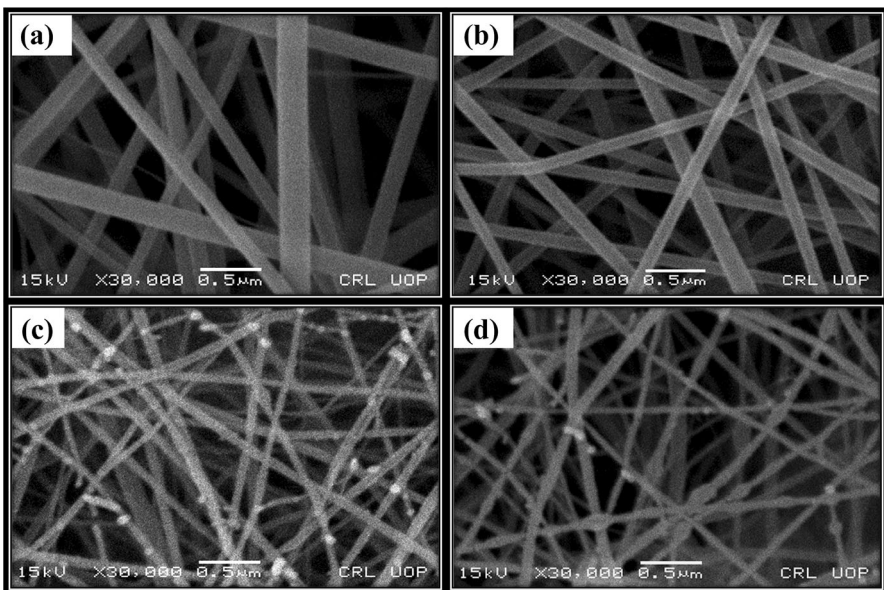
Fig. 2 SEM images of as prepared nanofibers **a** TiO₂, **b** 2.5 wt.%, **c** 5.0 wt.%, **d** 7.5 wt.% Ag-loaded TiO₂
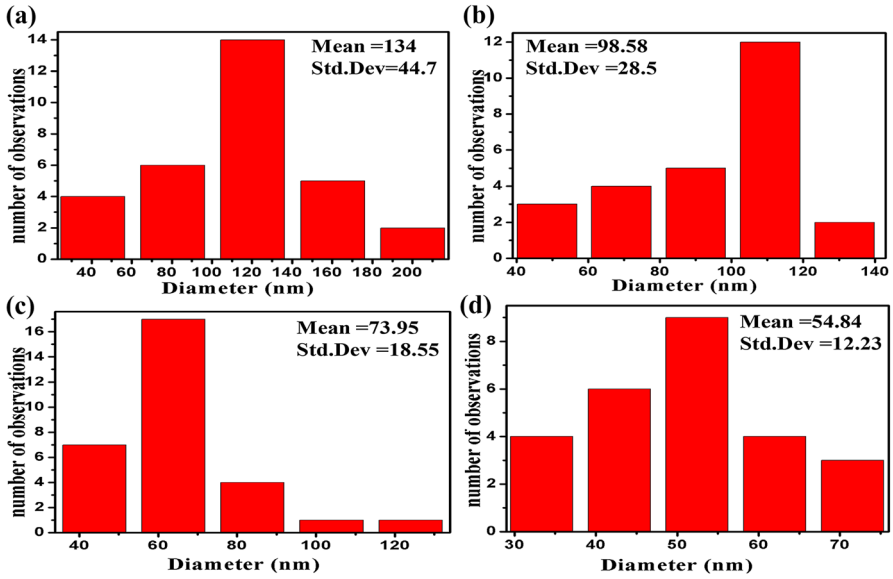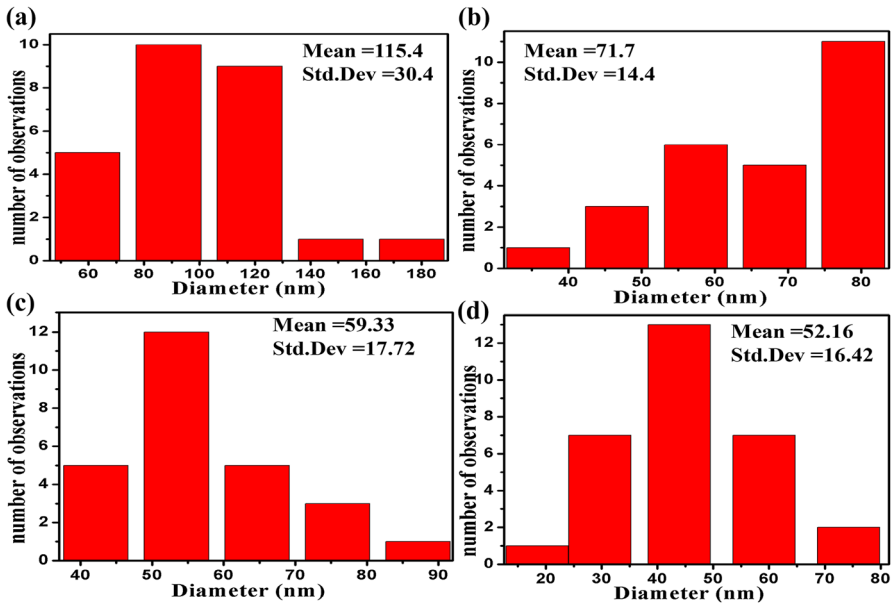
Fig. 3 Histogram of mean size distribution of as prepared nanofibers **a** TiO$_2$, **b** 2.5 wt.%, **c** 5.0 wt.%, **d** 7.5 wt.% Ag-loaded TiO$_2$
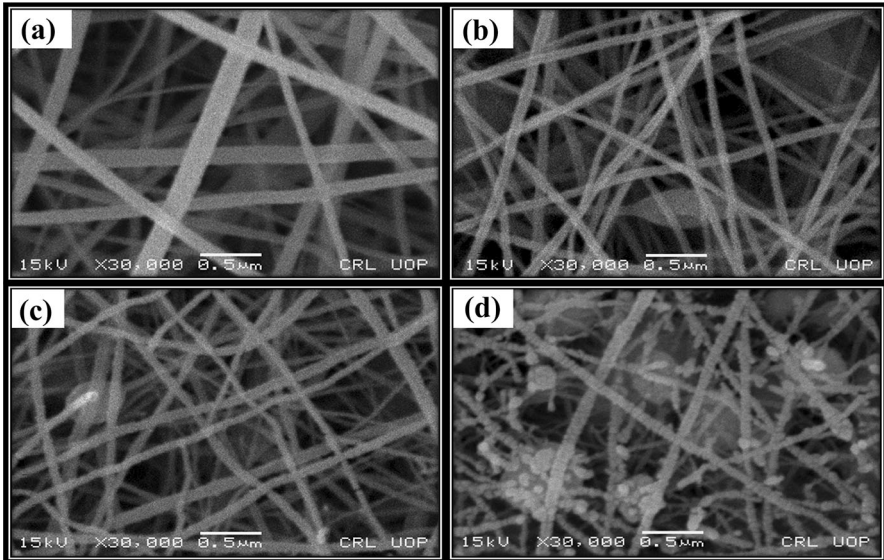
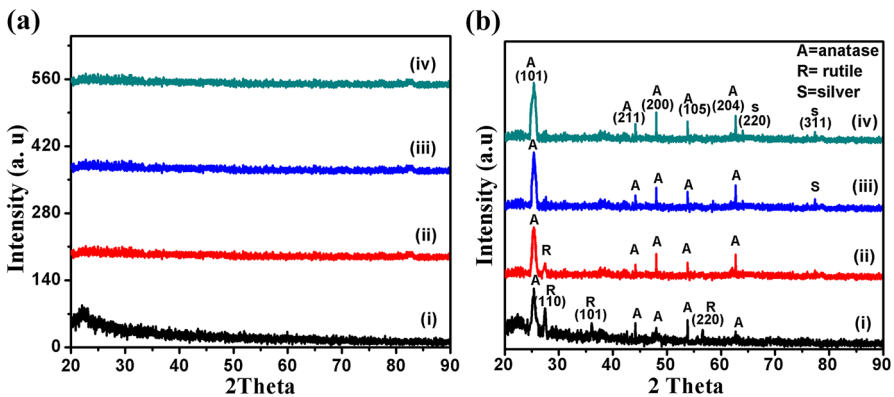

Fig. 4 SEM images of nanofibers calcined at 500 $^\circ$C **a** TiO$_2$, **b** 2.5 wt.%, **c** 5.0 wt.%, **d** 7.5 wt.% Ag-loaded TiO$_2$

degree of roughness on the outer surfaces of nanofibers has increased with loading of Ag and subsequent calcination. It is seen that with the increase of Ag loading, Ag nanoparticles are formed on the surface of nanofibers. The relative ratio of weight

Fig. 5 Histogram of mean size distribution of nanofibers calcined at 500 °C **a** TiO₂, **b** 2.5 wt.%, **c** 5.0 wt.%, **d** 7.5 wt.% Ag-loaded TiO₂

percentage of Ag/TiO₂ sample increased gradually, which indicated a more extensive coverage of TiO₂ nanofibers as shown in Fig. 4d. These Ag deposited nanoparticles on the fibers have also been confirmed by XRD as shown in Fig. 6b (iv). This can lead to have a positive influence on the photocatalysis due to the enhancement of active surfaces [16]. The histograms shown in Fig. 3 display the mean diameters of as-spun Ag-loaded TiO₂ nanofibers which have been found reduced from 134 to 55 nm with the Ag loading, while in the case of samples


Fig. 6 **a** XRD patterns of as prepared nanofibers, **b** XRD pattern of nanofibers calcined at 500 °C: (*i*) Pure TiO₂ (*ii*) 2.5 wt.% (*iii*) 5.0 wt.% (*iv*) 7.5 wt.% Ag-loaded TiO₂

calcined at 500 °C, mean diameter has shrunk from 115 to 52 nm. The variations in the mean diameters of both as-spun and calcined Ag-loaded nanofibers are shown in Fig. 7. The reduction in the mean diameters of Ag-loaded nanofibers has been attributed to the rise in the electrical conductivity of the polymer composite solution being electrospun, which has been ascribed to the presence of silver ions. The addition of silver nitrate ($AgNO_3$) improved the electrical conductivity of the polymer composite solution. Effusion of the silver nitrate loaded solution from the needle of the syringe in the strong electric field, which was established as a result of DC high voltage, lead to the formation of nanofibers that were vigorously stretched and pulled towards the collector plate as compared to those of the silver free solution. Moreover, the shrinkage in the diameter of heat treated samples with respect to the as-spun nanofibers owes to the removal volatile moieties such as PVP and ethanol, as well as the decomposition of titanium isopropoxide, [17]. The SEM micrographs show the surface morphology of the calcined nanofibers which grew rough as compared to the as-spun nanofiber samples. An interesting features observed in these SEM micrographs are the 1D nanostructures of the fibers which remained stable even up to the higher Ag loading.

X-ray Diffraction Analysis

The crystalline phases of the as-prepared and calcined samples were investigated by XRD analysis. Figure 6a indicates that no diffraction peak is observed in the as-spun nanofibers, depicting the amorphous nature of these samples. Figure 6b shows XRD patterns of samples which were calcined at 500 °C. Contrary to the as-spun nanofibers, calcined samples have shown a crystalline behavior. The pure TiO_2 nanofibers exhibit both A and R-phases, while the Ag-loaded TiO_2 samples have only the A-phase. The diffraction peaks appeared at 25.40°, 48.02°, 53.82°, 44.16° and 62.70° correspond to the (101), (200), (105), (211) and (204) crystalline planes
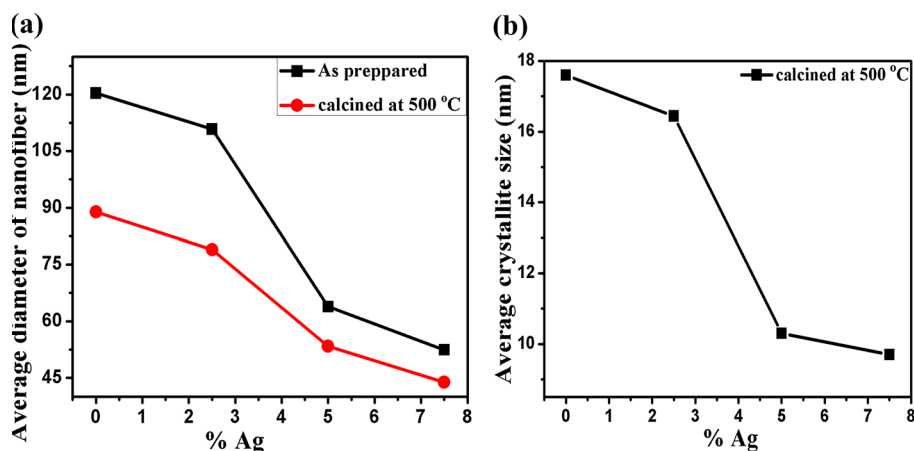
Fig. 7 **a** Mean diameter versus wt.% Ag loading of as prepared and calcined nanofibers. **b** Mean crystallite size versus wt.% Ag loading of calcined nanofibers

designating the A-phase, while the peaks observed at 27.45°, 36.09° and 56.64° corresponding to (110), (101) and (220) (pdf No. 01-083-2243) planes are attributed to R-phase [18]. The peaks at 64.02° and 77.36° correspond to (220) and (311) planes (pdf No. 01-071-4612) representing the Ag [19]. The concentrations of A and R-phases in the calcined samples have been determined by the Spurr equation [20].

$$X_A = \frac{100}{\left(1 + 1.265 \frac{I_R}{I_A}\right)} \tag{1}$$

where X_A is the percentage content of A-phase, I_A and I_R are the integral intensities of A(101) and R(110) peaks respectively. The crystallite size (D) has been calculated by using the Scherer's equation [21, 22].

$$D = \frac{k\lambda}{\beta \cos \theta} \tag{2}$$

where λ (0.154056 nm) is the wavelength of Cu K_α radiation, β is the full width at half maximum (FWHM) of diffracted peak and θ is the Bragg's angle. The mean crystallite size has been calculated to be decreasing with the increase of Ag contents in the TiO$_2$ nanofibers (Fig. 7). The reduction in mean diameter of nanofibers has been also supported by the SEM analysis.

By using the average crystallite size D, FWHM (β) and diffraction angle (θ), the dislocation density (δ) and strain in these nanofibers have been determined by using the following relationship [22, 23]

$$\delta = {}^1\!/_{D^2} \tag{3}$$

$$\varepsilon = {}^{\beta cos\theta}\!/_4 \tag{4}$$

The dislocation density is an estimation of number of defect lines per unit area (lines/nm^2) in a target material [24]. Table 1 shows the calculated values of dislocation density and micro strain which have been found heightening linearly with the rising Ag contents in TiO$_2$ matrix that ultimately inhibited the transformation of A-phase to R-phase. From these results, it has been noted that the Ag loading controlled the phase transformation in the TiO$_2$. There are two possible reasons which could be ascribed to the decrease in the phase transformation of TiO$_2$. Firstly, with the increase in Ag content, density of the surface defects in Ag-loaded TiO$_2$ nanofibers also boosts. This further lead to promote the process of phase transformation as surface defects are considered the nucleation sites for R-phase [25]. Secondly, surface oxygen vacancies' concentration of A-phase crystallites increased with the addition of Ag [19, 26], which favored the rearrangement of ions and reorganization of R-phase in the structure. Another attribute in this regard could be the domain mobility which is restricted due to the pinning of domain boundaries because of the crystal defects [27]. It is further believed that Ag contents which did not dissolve fully in the solvent, instead got accumulated at the grain boundaries. This has resulted into impeding the grain growth as well as reduction in the inter particle contact, which ultimately lead to

Table 1 Crystal structure parameters of Ag-loaded TiO$_2$ nanofibers calcined at 500 °C

Ag-loading in TiO$_2$ nanofibers (wt.%)	Anatase (%)	Anatase mean crystallite size (nm)	Rutile mean crystallite size (nm)	Mean crystallite size (nm)	Phase	(hkl)	Diffraction angle (2θ) (degree)	Dislocation density (δ) (10^{-3}) (lines/nm^2)	Micro strain (ε) (10^{-3})
TiO$_2$ (pure)	56	12.7	22.50	17.6	Anatase	(101)	25.40	6.20	2.72
					Rutile	(110)	27.44	1.97	1.50
2.5% Ag	76	11.9	20.98	16.44	Anatase	(101)	25.40	7.06	2.90
					Rutile	(110)	27.44	2.27	1.65
5.0% Ag	92	10.3	–	10.30	Anatase	(101)	25.40	9.42	3.36
7.5% Ag	99	9.7	–	9.70	Anatase	(101)	25.40	10.60	3.58

inhibition of phase transformation process from R to A-phase [28, 29]. The presence of Ag atoms in TiO2 matrix also controlled the crystalline phase transformation process, therefore estimated mean diameter of crystallites (A and R-phase) of Ag-loaded TiO2 nanofibers has been observed to be smaller than those of pristine TiO2 nanofibers [30]. According to Seery et al., when Ag is loaded in the TiO2 nanofibers, all of its contents cannot intercalate into the crystal structure of matrix but the fraction of these get deposited on the surfaces of nanofibers also. Another reason ascribed to this characteristic of nanostructure is relatively large size of Ag ionic radii (126 pm) as compared to Ti^{4+} (68 pm). Hence, Ag atoms when accumulate at the grain boundaries, are assumed to hamper the diffusion and atomic rearrangement processes, thus inhibiting the transformation of crystalline phase [31].

Fourier Transform Infrared Spectroscopy (FT-IR)

To examine the chemical composition, purity and bonding features of as-spun and calcined nanofibers, FT-IR analysis has been performed from 4000 to 400 cm^{-1}, as shown in the Fig. 8. The peak observed at 650 cm^{-1} corresponds to the Ti–O bond in both as-spun and calcined samples, which strongly supported the formation of TiO2 within the PVP/TiO2 composite nanofibers. The IR peaks of PVP in the FT-IR spectrum have been observed at 2928 cm^{-1} (anti-symmetric stretching mode of C–H), 2854 cm^{-1} (symmetric stretching mode of C–H), 1665 cm^{-1} (stretching mode of C=O) and 1288 cm^{-1} (stretching mode of C–N) respectively [32]. The broad peak shown in Fig. 8a ranging between 3000 and 3500 cm^{-1} corresponds to the O–H stretching vibration of hydroxyl group consequent upon the absorbed moisture. The absorption intensity bands appeared at 3404, 1665 and 735 cm^{-1} respectively have been observed to be shifting towards the lower wave numbers with the rise in Ag contents, demonstrating the formation of Ag–TiO2 nanocomposite system [33]. It has been observed that the absorption in the Ag loaded TiO2 nanofibers has slightly shifted towards the visible region. This is not only attributed to the metal
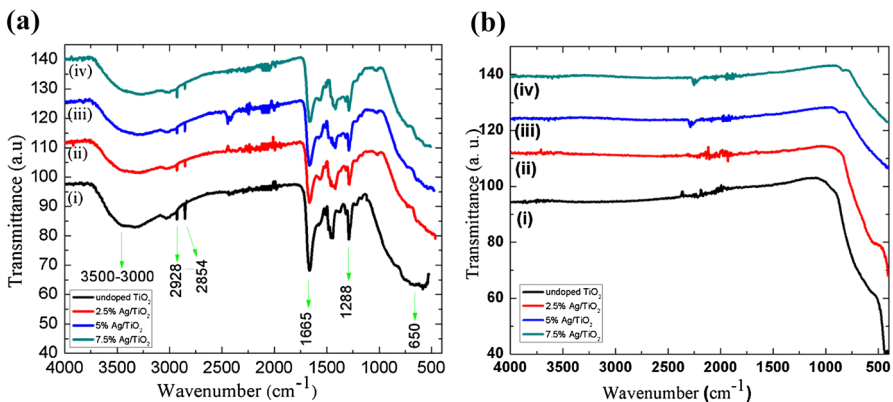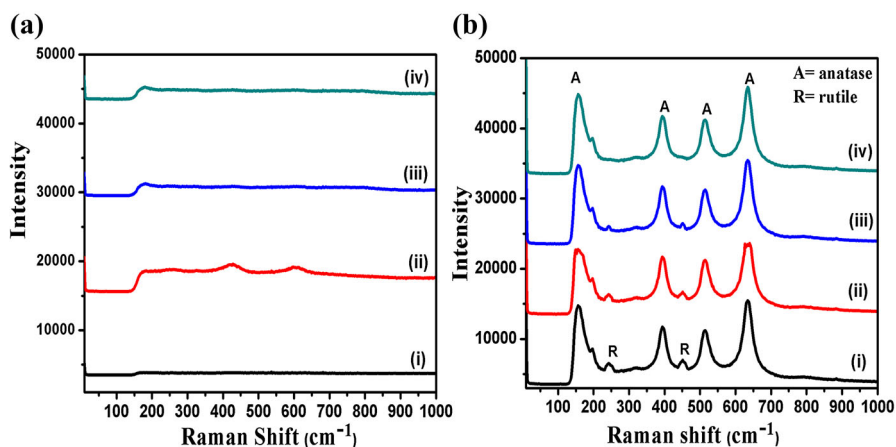

Fig. 8 **a** FT-IR spectra of as prepared and **b** nanofibers calcined at 500 °C of (*i*) TiO2, (*ii*) 2.5 wt.%, (*iii*) 5.0 wt.%, (*iv*) 7.5 wt.% Ag-loaded TiO2

clusters that give rise to the localized energy in the band gap but also believed to have taken place due to surface plasmon absorption owing to the presence of Ag nanoparticles [34]. This behavior is prominent especially in the nanofibers with higher weight percent (7.5 wt.%) loading of Ag, which has shown the largest red-shift. Figure 8b shows that peaks corresponding to PVP, ethanol, and water have completely been eliminated after calcination at 500 °C, illustrating removal of organic moieties. On the other hand, the strong absorption band of TiO_2 has appeared between 800 and 400 cm^{-1} which existed in the samples even after calcination. Moreover, the red-shift from 650 to 450 cm^{-1} in the peak of Ti–O stretching mode demonstrates the rearrangement in the crystal structure of TiO_2 from R to A- phase upon calcination [35].

Raman Spectroscopy

Raman spectroscopy (RS) is considered a highly sensitive technique used to investigate local and dynamic crystal structure symmetry in the materials. The evolution of R to A-phase in the crystalline structure of electrospun nanofibers of TiO_2 has been observed by Raman spectroscopy as a function of increasing Ag contents in the matrix. Figure 9a shows that no prominent Raman peaks could be observed in the as-prepared Ag-loaded TiO_2 nanofibers, rather minute fluctuations have been noted. This type of behavior in the as spun nanofibers was depicting that no crystal structure symmetry existed in them. Moreover, the structure of these samples was found to be amorphous, a characteristic which has also been supported by the XRD results. Nevertheless, prominent Raman peaks observed in the calcined nanofibers have illustrated the existence of crystalline structure, as shown in Fig. 9b. The four Raman vibration bands have been observed at 156 (E_g), 393(B_{1g}), 514 (A_{1g}) and 635 (E_g) cm^{-1} respectively ascribed to A-phase, whereas 244 (E_g), and 450 (A_{1g}) cm^{-1} illustrated the R-phase structures ranging between 100 and

Fig. 9 **a** Raman spectra of as prepared nanofibers and **b** nanofibers calcined at 500 °C of (*i*) TiO_2, (*ii*) 2.5 wt.%, (*iii*) 5.0 wt.%, (*iv*) 7.5 wt.% Ag-loaded TiO_2

1000 cm^{-1} [36, 37]. Here, the two Raman bands observed at 156 and 393 cm^{-1} are attributed to the O–Ti–O bending-type vibrations, while the other two modes having peaks at 514 and 635 cm^{-1} correspond to Ti–O bond stretching-type vibrations [38, 39]. A small peak (knee) observed at 196.5 cm^{-1} (E$_g$) has been assigned to the A-phase of TiO$_2$ [40]. The intensities of two relatively small R-phase peaks have been noted to be receding with the rising Ag content in the TiO$_2$ matrix, whereas the crystalline phase of nanofibers have transformed thoroughly to A-phase at 7.5 wt.% Ag loading. This indicates that Ag atoms facilitated the phase transformation of TiO$_2$ from R to A-phase. The sensitivity of Raman spectroscopy has been considered as a key reason that R-phase in TiO$_2$ nanofibers loaded with Ag has been distinguished which could not be differentiated by the XRD.

Conclusions

The effect of Ag loading and calcination on the crystal structure, phase transformation, morphology, vibrational phonon bands, chemical compositions and mean size distribution, on the TiO$_2$ electrospun nanofibers have been tailored, observed and estimated. The as spun nanofibers have been recognized as amorphous but exhibited high aspect ratio whereas samples calcined at 500 °C have shown good crystallinity and even surface morphology. The extent of roughness on the outer surfaces of calcined nanofibers has been found to increase with the Ag loading, that has been attributed to the formation of Ag nanoparticles which were adsorbed on the surface of these nanofibers. The mean diameter of nanofibers and average crystallite size have been found reduced while dislocation density and micro strain increased with the rise in Ag loading in the TiO$_2$ matrix. Reduction in mean size of nanofibers took place when organic moieties left the TiO$_2$ matrix after calcination. Further analysis of calcined nanofibers have revealed the thorough transformation of R-phase to A-phase in the samples loaded with 7.5 wt.% of Ag content. The loading of Ag at higher concentrations in these nanofibers has not destroyed the 1D structure which posses large active surface area required for many novel applications like photocatalysis, photovoltaic, and sensing.

References

1. D. A. Boyd, L. Greengard, M. Brongersma, M. Y. El-Naggar, and D. G. Goodwin (2006). *Nano Lett.* **6**, 2592–2597.
2. D. A. H. Hanaor and C. Charles (2011). Sorrell, review of the anatase to rutile phase transformation. *Mater. Sci.* **46**, 855–874.
3. T. B. Ghosh, S. Dhabal, and A. K. Datta (2003). *Appl. Phys.* **94**, 4577.
4. M. Hirano, N. Nakahara, K. Ota, O. Tanaike, and N. Inagaki (2003). *Solid State Chem.* **170**, 39.
5. G. Li, L. Li, J. G. Boerio, and B. F. Woodfield (2005). *Am. Chem. Soc.* **127**, 8659.
6. M. Xu, et al. (2011). Photocatalytic activity of bulk TiO$_2$ anatase and rutile single crystals using infrared absorption spectroscopy. *Phys. Rev. Lett.* **106**, 138302.
7. O. Carp, C. L. Huisman, and A. Reller (2004). *Prog. Solid State Chem.* **32**, 33–177.

8. Y. Dai, C. M. Cobley, J. Zeng, Y. Sun, and Y. Xia (2009). *Nano Lett.* **9**, 2455–2459.
9. S. J. Doh, C. Kim, S. G. Lee, S. J. Lee, and H. Kim (2008). *J. Hazard. Mater.* **154**, 118–127.
10. R. Kralchevska, M. Milanova, T. Tišler, A. Pintar, G. Tyuliev, and D. Todorovsky (2012). *Mater. Chem. Phys.* **133**, 1116–1126.
11. L. Han, Y. Xin, H. Liu, X. Ma, and G. Tang (2010). *J. Hazard. Mater.* **175**, 524–531.
12. A. Vohra, D. Goswami, D. Deshpande, and S. Block (2006). *Appl. Catal. B* **64**, 57–65.
13. D. Li and Y. Xia (2003). *Nano Lett.* **3**, 555–560.
14. R. Chandrasekar, L. Zhang, J. Y. Howe, N. E. Hedin, Y. Zhang, and H. Fong (2009). *J. Mater. Sci.* **44**, 1198–1205.
15. S. Chuangchote, J. Jitputti, T. Sagawa, and S. Yoshikawa (2009). *ACS Appl. Mater. Interfaces* **1**, 1140–1143.
16. G. Hongyu, W. Xiaohong, G. Yihang, and S. Changlu (2013). *Appl. Surf. Sci.* **280**, 720–725.
17. W. Chang, F. Xu, X. Mu, L. Ji, G. Ma, and J. Nie (2013). *Mater. Res. Bull.* **48**, 2661–2668.
18. H. E. Chao, Y. U. Yun, H. U. Xingfang, and A. Larbot (2003). *J. Eur. Ceram. Soc.* **23**, 1457–1464.
19. J. G. Amores, and V. S. Escribano (1994) *J. Mater. Chem.* **4**.
20. C. Suryanarayana and M. G. Norton *X-ray Diffraction: A Practical Approach* (Springer, Berlin, 2013).
21. R. A. Spurr and H. Myers (1957). *Anal. Chem.* **29**, 760–762.
22. R. E. Bailey, A. M. Smith, and S. Nie (2004). *Phys. E* **25**, 1–12.
23. N. K. Reddy, K. Ramesh, R. Ganesan, K. R. Reddy, K. Gunasekhar, and E. Gopal (2006). *Appl. Phys. A* **83**, 133–138.
24. M. Behnajady, N. Modirshahla, M. Shokri, and B. Rad (2008). *Glob. Nest J.* **10**, 1–7.
25. B. M. Reddy, G. K. Reddy, K. N. Rao, I. Ganesh, and J. M. Ferreira (2009). *J. Mater. Sci.* **44**, 4874–4882.
26. D. Vu, X. Li, Z. Li, and C. Wang (2012). *J. Chem. Eng. Data* **58**, 71–77.
27. J.-Y. Park, K.-J. Hwang, J.-W. Lee, and I.-H. Lee (2011). *J. Mater. Sci.* **46**, 7240–7246.
28. T. M. Khan and T. BiBi (2012). *Chin. Phys. B* **21**, 097303.
29. C. Rath, P. Mohanty, A. Pandey, and N. Mishra (2009). *J. Phys. D Appl. Phys.* **42**, 205101.
30. H. C. Wu *Continuum Mechanics and Plasticity* (CRC Press, Boca Raton, 2004).
31. A. Alves, F. Berutti, F. Clemens, T. Graule, and C. Bergmann (2009). *Mater. Res. Bull.* **44**, 312–317.
32. S. Ray, R. Banerjee, and A. Barua (1980). *Jpn. J. Appl. Phys.* **19**, 1889.
33. M. Suwarnkar, R. Dhabbe, A. Kadam, and K. Garadkar (2014). *Ceram. Int.* **40**, 5489–5496.
34. T. Ohsaka, F. Izumi, and Y. Fujiki (1978). *J. Raman Spectrosc.* **7**, 321–324.
35. S. Hamaguchi and H. Yoshitake (2009). *Electrochemistry* **77**, 373–378.
36. A. N. Murashkevich, A. S. Lavitskaya, T. I. Barannikova, and I. M. Zharskii (2008). *J. Appl. Spectrosc.* **75**, 730–734.
37. X. Feng, X. Wang, X. Chen, and Y. Yue (2011). *Acta Mater.* **59**, 1934–1944.
38. M. R. Hoffmann, S. T. Martin, W. Choi, and D. W. Bahnemann (1995). *Chem. Rev.* **95**, 69–96.
39. J. Zhang, M. Li, Z. Feng, J. Chen, and C. Li (2006). *J. Phys. Chem. B* **110**, 927–935.
40. S. Vlassov, B. Polyakov, M. Vahtrus, M. Mets, M. Antsov, R. Saar, and L. Dorogin (2015). *Mater. Charact.* **100**, 98–103.